Applied Catalysis B: Environmental 324 (2023) 122169

Contents lists available at ScienceDirect

Applied Catalysis B: Environmental

journal homepage: www.elsevier.com/locate/apcatb

Cooperative hydrogen evolution reaction combining $Cu_{2+1}O$ and Ru active sites

Jing Wang [a,*], Bingxin Guo [a], Junting Sun [a], Yingshuang Zhou [a], Chengfei Zhao [a], Zhongzhe Wei [b,*], Junjie Guo [a,*]

[a] College of Materials and Environmental Engineering, Institute of Advanced Magnetic Materials, Hangzhou Dianzi University, Hangzhou 310018, China
[b] Institute of Industrial Catalysis, College of Chemical Engineering, Zhejiang University of Technology, Hangzhou 310032, China

ARTICLE INFO

Keywords:
Hydrogen evolution reaction
Electrocatalyst
$Cu_{2+1}O$
Multi-component
Synergistic effect

ABSTRACT

The design and construction of electrocatalysts with multiple components to modulate the intrinsic catalytic activity is a compelling strategy to achieve Pt-like activity for hydrogen generation. Challenging on the inert Cu-based electrocatalysts for water reduction, herein, a novel and fruitful CuRu-based electrocatalysts ($RuCuO_x$/NC) is established by combining dual-templates assembling and pyrolysis protocol with a subsequent hot-alkali corrosion. Benefitting from the synergetic effect of $Cu_{2+1}O$ (with copper excess defects) and Ru, the as-prepared $RuCuO_x$/NC affords brilliant activity and stability under alkaline condition. In 1 M KOH, the $RuCuO_x$/NC provides Pt-like activity with overpotential of ~29 mV to reach 10 mA cm^{-2}. Theoretical calculations certified that H_2O dissociation was accelerated and hydrogen adsorption free energy was optimized by the cooperation of $Cu_{2+1}O$ and Ru. This work proposes a promising methodology to construct multi-components electrocatalysts, which may lend perspective for the design of advanced electrocatalysts for renewable energy systems.

1. Introduction

Hydrogen (H_2), as an ideal energy carrier with abundant sources, eco-environmental and zero-carbon emission, plays a pivotal part in ammonia synthesis and new energy vehicles industries [1,2]. The vigorous development of green H_2 has changed the energy structure of the world today [3], and thus has become the inevitable choice to break through the bottleneck of resources and environment. Undoubtedly, H_2 production by green synthetic process is the key step affecting economic development. Compared with traditional hydrogen synthetic approaches, such as natural gas reforming and coal gasification, water electrolysis fundamentally solves the dependence on fossil fuels and realizes the conversion from H_2O to high-purity H_2 [4]. Despite tremendous efforts have been devoted, sustainable and efficient H_2 production via hydrogen evolution reaction (HER) is still hampered by the lack of advanced and robust cathode materials [5–8]. Compared with HER under acid media, HER in alkaline media delivered sluggish kinetics owing to an additional H-OH dissociation energy barrier [9]. Nevertheless, the commercialization of hydrogen production under acid is prohibited by the limited rate of oxygen evolution at the counter electrode of HER [10]. Therefore, it is imperative to exploit alkaline HER electrocatalysts with remarkable performance for the development of large-scale hydrogen economy [11–13].

Cost and catalytic performance are the first principles for the design of advanced electrocatalysts. Although Pt-based materials are considered the state-of-the-art HER catalysts, the severe scarcity and inconvenient mining of Pt lead to the exorbitant price, which seriously hindered their extensive applications [14]. To perform H_2 production in an economic manner, the development of high-activity and cost-effective alternatives becomes one of the leading research frontiers in the electrocatalytic field. According to the Brewer-Engel theory, the transition metals with empty d electrons or d empty orbital are conductive to HER [15]. Over the recent decades, the exploit of earth-abundant transition metal-based electrocatalysts for HER, involved Co-, Fe-, Ni-, Mo-based electrocatalysts, presents a piece of prosperous scene [16–24]. However, it is rarely reported that Cu with full d electrons of $3d^{10}4s^1$ can presents a satisfied performance. Moreover, metallic Cu possesses weak binding capacity for H* (ΔG_{H^*}) via the Nørskov volcano theory [25], which lowers HER efficiency. Actually, Cu-based catalysts for HER were scantly reported. Thus, designing

* Corresponding authors.
E-mail addresses: chemwj@hdu.edu.cn (J. Wang), weizhzhe@zjut.edu.cn (Z. Wei), jguo@hdu.edu.cn (J. Guo).

https://doi.org/10.1016/j.apcatb.2022.122169
Received 27 July 2022; Received in revised form 13 October 2022; Accepted 9 November 2022
Available online 19 November 2022

high-performance Cu-based electrocatalysts is both an opportunity and challenge. As an effective strategy to accommodate the intrinsic activity, multi-component synergistic engineering has been carried out for encouraging achievements in recent years [26]. It is feasible to modify the electronic structure of the host metal by introducing a second or third active component to optimize H* bonding strength, thereby promoting the intrinsic catalytic capability [27,28]. In particular, metal Ru has attracted intense attention by researchers in virtue of the theoretically high intrinsic activity with a Ru-H strength similar to that of Pt-H bond [29], but with much low price [30,31]. It is suggested that Ru, which serves as the regulator to optimize the ΔG_{H^*}, is an ideal alternative for obtaining competitive catalytic performance [32–38]. Even so, the fundamental design of high-performance CuRu-based electrocatalysts is still in its infancy [39,40], which could usher in unprecedented development opportunities for researchers to construct high-activity Cu-based electrocatalysts.

Herein, a novel and high-efficiency CuRu-based electrocatalyst ($RuCuO_x$/NC) was constructed by combining dual-templates assembling and pyrolysis strategy with a subsequent hot-alkali etching. The formed polygonal Cu/$Cu_{2+1}O$ nanoparticles are attached with uniformly dispersed Ru nanoparticles to form opulent cooperative interfaces. Notably, the hot-alkali etching affords the “killing three birds with one stone”: i) transforming dense Cu nanowires to polyhedral Cu-based nanoparticles by chemical oxidation reaction; ii) promoting the formation of active $Cu_{2+1}O$ phase; iii) removing SiO_2 to create mesopores. Benefitting from the synergistic effect between $Cu_{2+1}O$ and Ru, the $RuCuO_x$/NC displayed brilliant activity and stability under alkaline medium. To reach 10 mA cm^{-2}, $RuCuO_x$/NC delivered an overpotential of ~29 mV. Density functional theory (DFT) calculation results further corroborated that the cooperative effect of $Cu_{2+1}O$ and Ru significantly accelerated H_2O dissociation and moderated the ΔG_{H^*}. This work gives a fresh impetus to construct advanced alternatives for efficient water reduction.

2. Experimental section

2.1. Chemicals

Ruthenium (III) chloride (RuCl3), D-Glucosamine hydrochloride (GAH), urea, Hexadecyl trimethyl ammonium bromide (CTAB), ethanol, NaOH were purchased from Aladdin. Ludox and Nafion solution were obtained from Sigma-Aldrich Trading Co., Ltd (USA). $Cu(NO_3)_2\cdot 3H_2O$ was purchased from Macklin biochemical technology Co., Ltd. All the chemicals were of analytical grade and directly used without further purification.

2.2. Synthesis of materials

Taking the fabrication of $RuCuO_x$/NC as an example, 1 g GAH, 0.5 g urea, 0.25 g CTAB, and 0.291 g $Cu(NO_3)_2\cdot 3H_2O$ were dissolved in 60 mL deionized water. Then, 0.8 mL $RuCl_3$ solution, where Ru content was 10 mg mL^{-1}, was dispersed in the mixture. After magnetic stirring for a while, Ludox was introduced and along with refluxing at 60 °C. Whereafter, the homogeneous mixture was transferred in PTFE vessel purchased from Anhui Kemi Machinery Technology Co., Ltd. and was sealed, which was reacted at 200 °C for 10 h. The resulting product (marked as $RuCuO_x$/NC-H) was separated by suction filtration and repeatedly washed with deionized water and then dried under vacuum for overnight. Subsequently, $RuCuO_x$/NC-H was grinded into powder, and annealed in tube furnace under N_2 flow (named as $RuCuO_x$/NC-P). The detailed calcination procedure was as follows: elevating the pyrolysis temperature from room temperature to 600 °C for 1 h at a ramping rate of 10 °C min^{-1}, and further elevating to 800 °C for 1 h. Finally, $RuCuO_x$/NC was obtained after treating $RuCuO_x$/NC-P with NaOH under 70 °C.

For comparison, NC was synthesized via the similar procedure without the addition of $Cu(NO_3)_2\cdot 3H_2O$ and $RuCl_3$. As for Ru/NC and CuO_x/NC, they were fabricated by the similar procedure of $RuCuO_x$/NC without the addition of $Cu(NO_3)_2\cdot 3H_2O$, $RuCl_3$, respectively.

$Ru_{0.05}CuO_x$/NC and $Ru_{0.1}CuO_x$/NC were prepared with the similar process of $RuCuO_x$/NC except for the Ru element dosage as 0.05 mmol and 0.1 mmol, respectively.

$RuCuO_x$/NC-60 and $RuCuO_x$/NC-80 were prepared with the similar process of $RuCuO_x$/NC except for the temperature reacting with NaOH changed to 60 °C and 80 °C, respectively.

0.1 g $RuCuO_x$/NC was dispersed into 2 M, 50 mL H_2SO_4 solution. And then the above mixture stirred continuously at room temperature for 120 h. Subsequently, the mixture was washed with deionized water and filtered until the filtrate was neutral. Finally, the product was dried in vacuum and ground into powder to obtain $RuCuO_x$/NC-Acid.

0.05 g $RuCuO_x$/NC was put into a tube furnace, which was programmed at 250 °C for 4 h with a heating rate of 10 °C min^{-1}. After that, $RuCuO_x$/NC-H_2 was obtained after the tube furnace cooling to room temperature under H_2 flow.

2.3. Characterizations

High-resolution transmission electron microscopy (HRTEM) was utilized for the research of the inner nanostructures, which operated on Tecnai G2 F30 S-Twin at an acceleration voltage of 300 KV. The metal phase of samples was tested with a slit width of 5 mm on a D/tex Ultima TV wide angle X-ray diffractometer (XRD) equipped with Cu Kα radiation source (1.54 Å), and a phase of 10° to 90° sweep data at a sweep rate of 5° min^{-1}. Electron paramagnetic resonance (EPR) was measured under room temperature on a Bruker A300. H_2 temperature programmed reduction (H_2-TPR) experiment was carried out on a programmed temperature chemisorption apparatus (BelCata II, Japan). Element contents were measured on a elemental analyzer (Elementar, UNICUBE). The Raman spectra were performed on a Raman spectrometer (Renishaw, Invia). The specific surface area (SSA) and pore size distribution (PSD) plot were calculated by the conventional Brunauere-Emmette-Teller (BET) and BJH method, respectively. The Thermo ESCALAB 250xi spectrometer was employed to obtain X-ray photoelectron spectra (XPS) and X-ray induced Auger electron spectroscopy (XAES) for the analysis of bonding states and surface chemistry. Cu and Ru *K*-edge analysis was performed with Si (311) crystal monochromators at the BL14W1 beamlines of the Shanghai Synchrotron Radiation Facility (SSRF) (Shanghai, China). ICP-OES analysis was recorded on Aglient 5110 spectrometer to probe the contents of Ru and Cu. $RuCuO_x$/NC was completely dissolved by microwave digestion before testing. The Ru and Cu content was measured to be 2.40 wt% and 24.85 wt%, respectively.

2.4. Electrochemical measurements

The electrochemical experiments were performed in a typical three-electrode configuration at room temperature by an electrochemical workstation of CHI760E. Glassy carbon electrode (5 mm in diameter), graphite rod and saturated calomel electrode (SCE) were utilized as working electrode, counter electrode, and reference electrode severally. Briefly, 3 mg catalyst was ultrasonically dispersed in the mixture of Nafion (20 μL) and ethanol (300 μL). Afterward, the uniform catalyst slurry (30 μL) was drop-cast onto the surface of the glassy carbon electrode and naturally dried in the air. Linear sweep voltammetry (LSV) curves were recorded under 1 M KOH and 1 M PBS solution with a sweep rate of 5 mV s^{-1}. All the polarization curves were collected with iR correction. From LSV data, the corresponding overpotential was obtained. Besides, the Tafel slope was fitted by the Tafel equation ($\eta = a + b\log(j)$), where b represented the Tafel slope. The electrochemical impedance spectroscopy (EIS) was measured frequencies from 100 kHz to 0.01 Hz. To determine the electrochemical active surface area (ECSA) of the samples, a series of cyclic voltammetry (CV) curves were recorded

at multiple scan rates ranging from 10 to 50 mV s^{-1} in the non-Faradaic region. The geometric double layer capacitance (C_{dl}) was calculated by plotting the difference of current density $\Delta J = (J_{anodic} - J_{cathodic})/2$ at 0.15 V vs. RHE against the scan rate. To evaluate the stability, continuous 3000 CV scanning tests between 0.1 ~ − 0.4 V (vs. RHE) were performed.

2.5. DFT calculation details

All of calculations were carried out within the framework of the

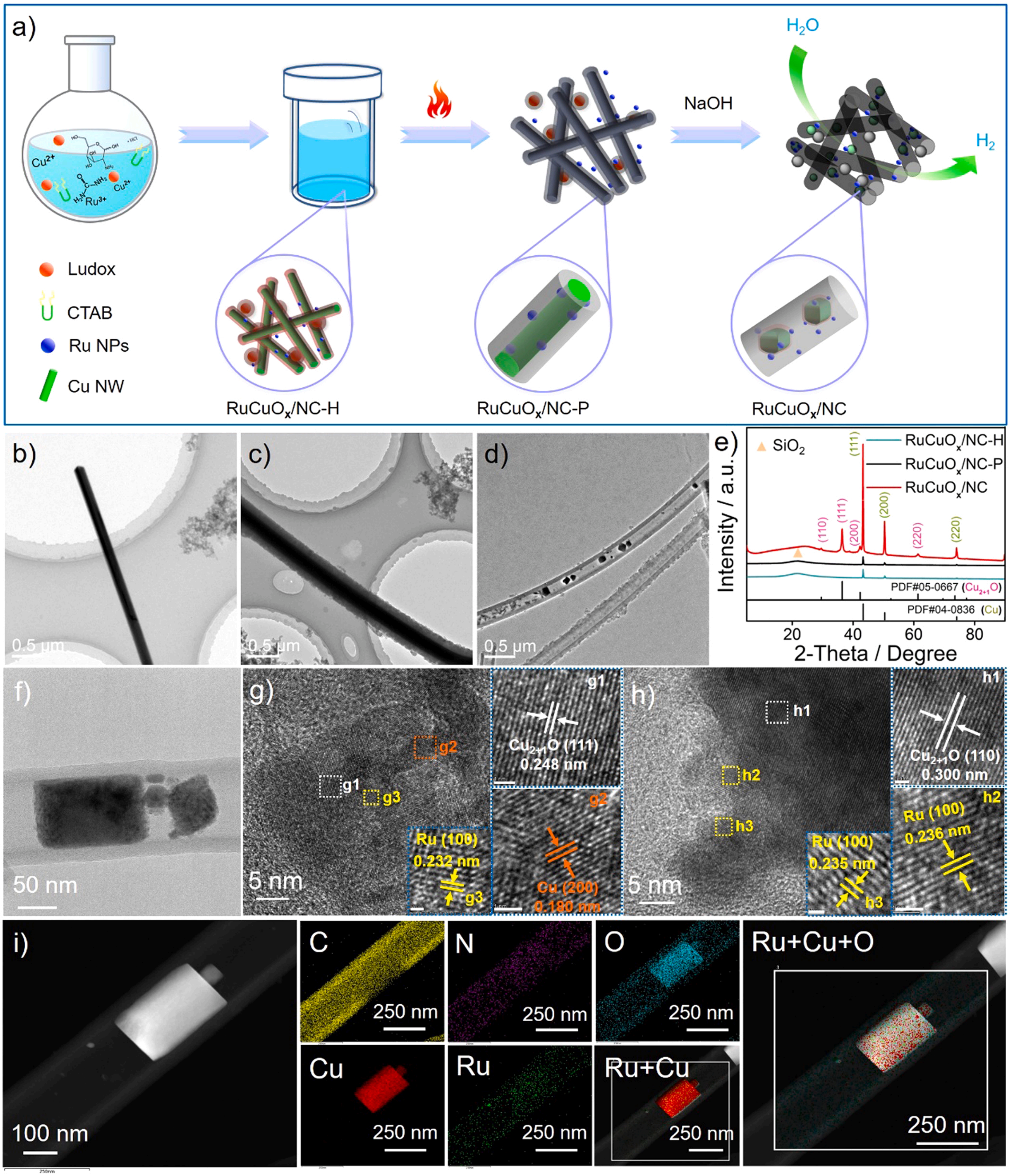

Fig. 1. a) Schematic illustration of the fabrication of RuCu-based electrocatalysts, b) TEM images of $RuCuO_x$/NC-H, c) TEM images of $RuCuO_x$/NC-P, d) TEM images of $RuCuO_x$/NC, e) XRD pattern of $RuCuO_x$/NC-H, $RuCuO_x$/NC-P, $RuCuO_x$/NC, f) TEM image of $RuCuO_x$/NC, g-h) HRTEM images of $RuCuO_x$/NC, g1-g3, h1-h3 HRTEM images of the corresponding zones in g and h, the scale bar of g1, g2, h1, h2 was 1 nm, the scale bar of g3, h3 was 500 pm, i) Elemental mapping.

generalized gradient approximation (GGA) with the Perdew-Burke-Ernzerhof (PBE) functional in the Vienna ab initio simulation package (VASP). The effect of van der Waals interaction is significant for the reaction mechanism in our precious study. Therefore, the DFT-D3 method was utilized to calculate all the free energy. The projector-augmented-wave (PAW) method was utilized to describe the core-valence electron interaction, and the cutoff energy of plane-wave basis expansion was set at 450 eV. A $3 \times 3 \times 1$ Monkhorst-Pack *k*-point mesh sampling was employed for three model systems, namely Ru/Cu, Ru/CuO, Ru/Cu_2O and Ru/$Cu_{2+1}O$ severally. Cu (111), CuO (111) and Cu_2O (111) surface was chosen as the support for those systems. For consistence with experiment, we constructed oxygen vacancies through removing oxygen atoms on the perfect Cu_2O (111) anatase surface to simulate Ru/$Cu_{2+1}O$. All surfaces were built using periodic slabs of four layers. The bottom two layers of atoms were fixed, and the top two layers were relaxed with a 15 Å vacuum region.

3. Results and discussion

3.1. Synthesis of $RuCuO_x$/NC

In this study, nitrogen-containing biomass glucosamine hydrochloride (GAH) was functioned as C source and N source. Ludox and Hexadecyl trimethyl ammonium bromide (CTAB) as dual-templates served as structure-directing agent of active metal and pore-forming agent of carbon matrix. The synthetic process of $RuCuO_x$ supported on nitrogen doped carbon ($RuCuO_x$/NC) was described in Fig. 1a. $RuCuO_x$/NC-H and $RuCuO_x$/NC-P represented the samples collected after hydrothermal reaction and pyrolysis severally. Under the hydrothermal process (Fig. 1b and Fig. S1), CTAB acted as a structure-directing agent to assist the one-dimensional growth of Cu nanowires [41], during which, GAH adsorbed on the Cu nanowires and underwent thermal polymerized to form carbon layers coating on the outside. Meanwhile, Ru precursor nucleated and distributed uniformly on the surface of Cu nanowires. In addition, accumulated carbon nanospheres were also formed due to the inheritance of the Ludox structure. Transmission electron microscopy (TEM) analysis unambiguously revealed the composite skeleton architecture and element distribution of $RuCuO_x$/NC-P is similar to that of $RuCuO_x$/NC-H (Fig. 1c and Fig. S2). Upon treated with hot-alkali, Ludox template was removed to create mesopores. Unexpectedly, Cu nanowires were etched into polyhedral structure, which were confined in the carbon nanotubes (Fig. 1d and Fig. S3). In order to figure out the evolution of metallic phases during the growth of composites, the powder X-ray diffraction (XRD) was then performed. In accordance with the XRD patterns (Fig. 1e), only the diffraction peaks of metallic Cu and SiO_2 were observed for $RuCuO_x$/NC-H and $RuCuO_x$/NC-P. Upon post-treatment with NaOH, the diffraction peaks of SiO_2 vanished, indicating the complete removal of SiO_2. Moreover, XRD analysis

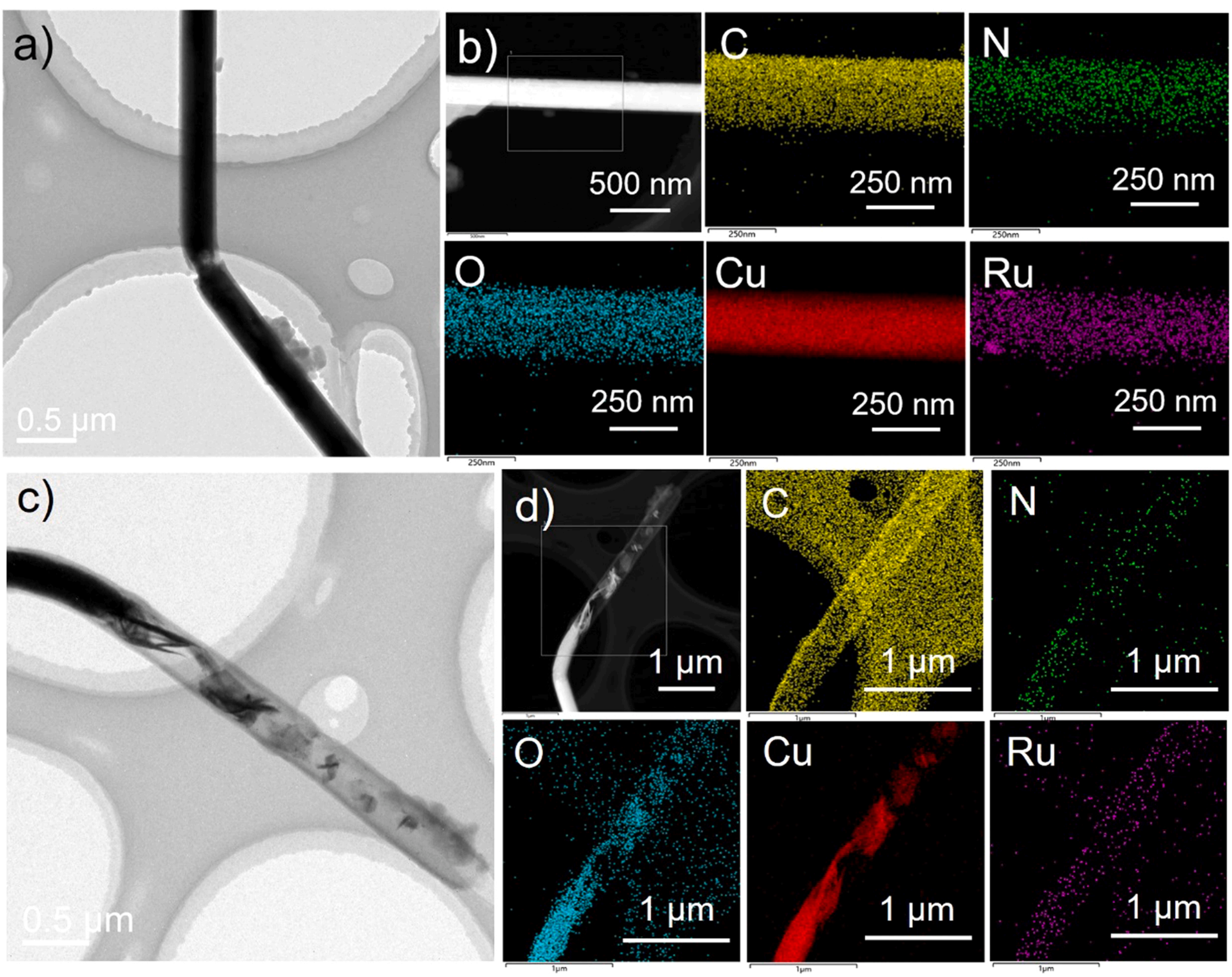

Fig. 2. a) TEM image of $RuCuO_x$/NC-nL, b) Elemental mapping for $RuCuO_x$/NC-nL, c) TEM image of $RuCuO_x$/NC-nL treated by NaOH, d) Eelemental mapping for $RuCuO_x$/NC-nL treated by NaOH.

unequivocally manifested that the diffraction peaks centered at ∼29.5°, ∼36.4°, ∼42.3 °, ∼61.3° can be indexed to (110), (111), (200), (220) planes of $Cu_{2+1}O$. That is, the distinctive $Cu_{2+1}O$, which featured copper excess defects, were introduced in $RuCuO_x/NC$ after thermo-alkali process. The new generated $Cu_{2+1}O$ may give rise to a reinforcement effect on the catalytic activity.

In order to further verify the formation mechanism of the catalysts, control samples without Ludox (denoted as $RuCuO_x$/NC-nL) or CTAB (denoted as $RuCuO_x$/NC-nC) template were synthesized by the similar process. From Fig. 2a-b, $RuCuO_x$/NC-nL presented a composite structure of carbon nanotubes filled with Cu nanowires. As expected, the obvious etching of Cu nanowires was observed after the thermo-alkali treatment (Fig. 2c-d). This phenomenon was consistent with the formation process of $RuCuO_x/NC$, further confirming NaOH treatment enabled the transformation of dense Cu nanowires to polyhedral Cu-based nanoparticles. In terms of the effect of CTAB, as can be seen from Figure S4, $RuCuO_x$/NC-nC exhibited a large range of granular bulk structure. Almost no tubular structures were observed in the absence of CTAB, confirming the guiding effect of CTAB. Moreover, Ru particles were seriously agglomerated without CTAB adding (Figure S5). More importantly, metallic Cu was etched violently during NaOH treatment in the absence of the effective umbrella of carbon layers. As a result, the Cu loading was significantly reduced after thermo-alkali corrosion. XRD analysis further revealed the aggregation of metallic Ru nanoparticles, which proving by the obvious diffraction peaks attributed to metallic Ru (Figure S6). Moreover, no observable Cu or $Cu_{2+1}O$ characteristic peaks presented, suggesting most Cu species were etched. The XRD results matched well with the TEM data. Therefore, CTAB not only played the role of structural inducer and metal dispersant, but also has a protective and stable effect on metallic Cu. From the above experimental results, it is reasonable to believe that the dual-templates played a crucial role in dispersing and stabilizing metals phase.

More morphological information of $RuCuO_x/NC$ was obtained via high-resolution transmission electron microscopy (HRTEM) (Fig. 1, Figure S7). As observed in Fig. 1f, there was noticeable carbon nanotube with compact walls presenting in $RuCuO_x/NC$. From the HRTEM (Fig. 1g-h) images, the lattice distances measured to be 0.244 nm and 0.300 nm were assigned to the (111) and (110) facets of $Cu_{2+1}O$, respectively. The lattice spacing was measured to be ∼0.180 nm, belonging to the (200) crystal planes of metallic Cu (Fig. 1g and Figure S7). More significantly, a large number of ultrafine Ru nanoparticles were concentrated near $Cu_{2+1}O$. Elemental mapping results further visualized that element C, N, O were evenly distributed throughout the carbon framework (Fig. 1i). Moreover, the overlap of element Cu and Ru mapping indicated that element Ru was preferentially dispersed on the $Cu_{2+1}O$ surface, which was nicely consistent with the HRTEM images and suggested the interplay between Ru and $Cu_{2+1}O$.

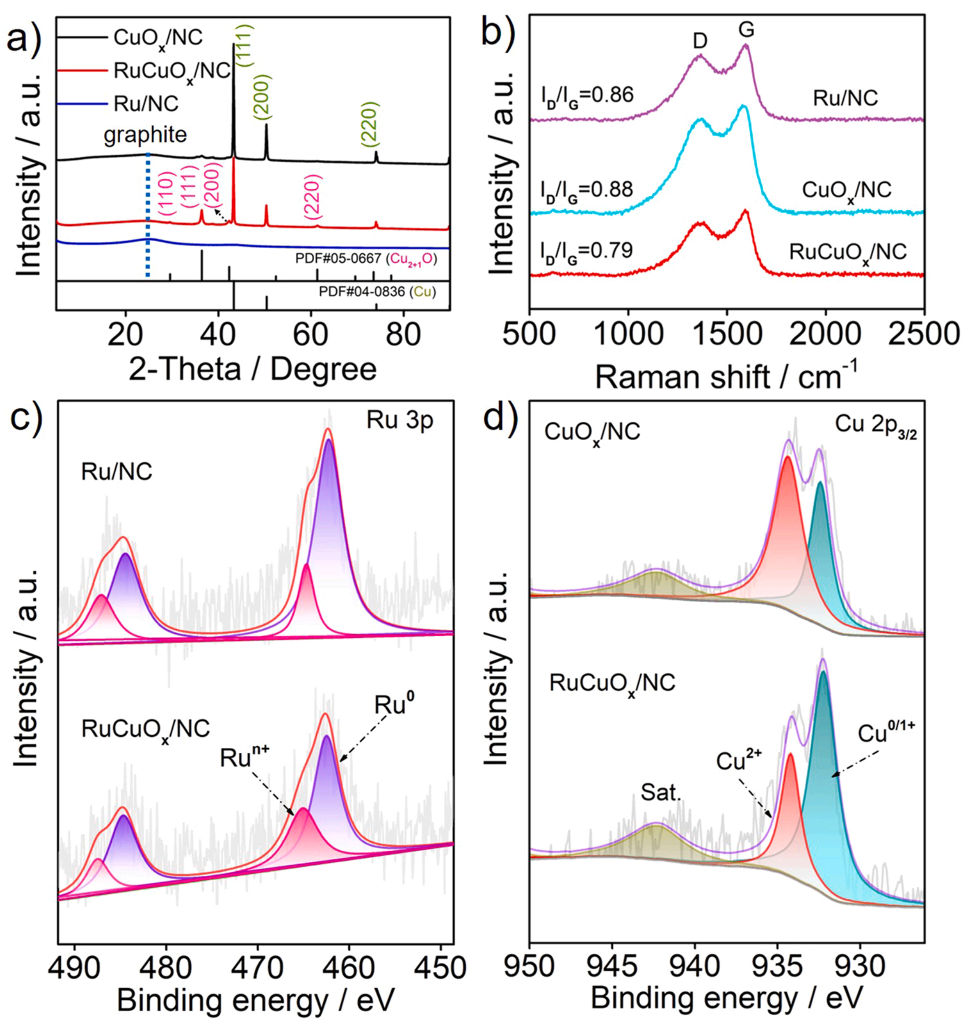

Fig. 3. a) XRD patterns of CuO_x/NC, Ru/NC and $RuCuO_x/NC$, b) Raman spectra of CuO_x/NC, Ru/NC and $RuCuO_x/NC$, c) Ru 3p XPS spectra of Ru/NC and $RuCuO_x/NC$, d) Cu $2p_{3/2}$ XPS spectra of CuO_x/NC and $RuCuO_x/NC$.

3.2. Structure characterizations

H_2-TPR experiment was further performed to reveal the interplay between of Ru and $Cu_{2+1}O$. As displayed in Figure S8, the H_2 consumption peak locating at ~228 °C corresponded to the reduction of CuO_x [42,43]. In addition, there were two weak H_2 consumption peaks at ~84 °C and ~131 °C with regard to $RuCuO_x$/NC, which were attributed to the reduction of ruthenium oxides [44]. It is remarkable that the reduction temperature of CuO_x obviously shifted to ~257 °C as Ru was introduced in the system. This result was caused by the interaction between Ru and $Cu_{2+1}O$, which led to the elevated reduction temperature [43]. Compared to the reference sample of CuO_x/NC without Ru, the obvious diffraction peaks of $Cu_{2+1}O$ for $RuCuO_x$/NC suggested that the introduction of Ru assisted the formation of $Cu_{2+1}O$ to a certain extent (Fig. 3a). Additionally, the absence of diffraction peaks of Ru phase manifested the formation of ultrafine Ru nanoparticles in $RuCuO_x$/NC, which matched well with the HRTEM data. Benefitting from the pore-creating effect of templates, $RuCuO_x$/NC exhibits the mesoporous feature, evidenced by a typical IV-type hysteresis ring [45], and the Brunauer-Emmett-Teller specific surface area was calculated to be 236 m^2 g^{-1} (Figure S9). Whereas, $RuCuO_x$/NC-nL exhibited much lower specific surface area compared with $RuCuO_x$/NC (Table S1). Additionally, the pore size distribution diagram indicated $RuCuO_x$/NC with a hierarchical porous architecture, which was conductive to the exposure of more active sites and the diffusion of reactants, thus may boost the catalytic property. Raman spectra were then conducted to uncover the degree of graphitization, which related to the electrical conductivity. As illustrated in Fig. 3b, specific D- and G-bands were presented. The intensity ratios of D/G (I_D/I_G) for $RuCuO_x$/NC, Ru/NC, CuO_x/NC were calculated as 0.79, 0.86, 0.88, respectively. The low I_D/I_G value of $RuCuO_x$/NC implied the high degree of graphitization, owing to the increased sp^2 graphitic structure [46]. Such structural feature contributed to the superior electroconductivity, which may accelerate the electrochemistry process.

To clarify the function of Ru on Cu-based phases, the chemical configuration and the surface electronic states of Ru, Cu constituents were traced by X-ray photoelectron spectroscopy (XPS). In Ru 3p spectrum, two-fitted peaks at ~462.27 eV and ~484.47 eV were corresponded to Ru^0 and the rest peaks were belonged to Ru^{n+} state (Fig. 3c) [32]. In addition, the Cu $2p_{3/2}$ spectra were deconvoluted into two peaks at ~932.2 eV, and ~934.2 eV, which were assigned to $Co^{0/1+}$ and Cu^{2+}, respectively (Fig. 3d) [47]. By studying the Cu $2p_{3/2}$ XPS spectra of CuO_x/NC and $RuCuO_x$/NC, together with the Ru 3p XPS spectra of Ru/NC and $RuCuO_x$/NC, it can be seen that the Ru 3p spectrum moved

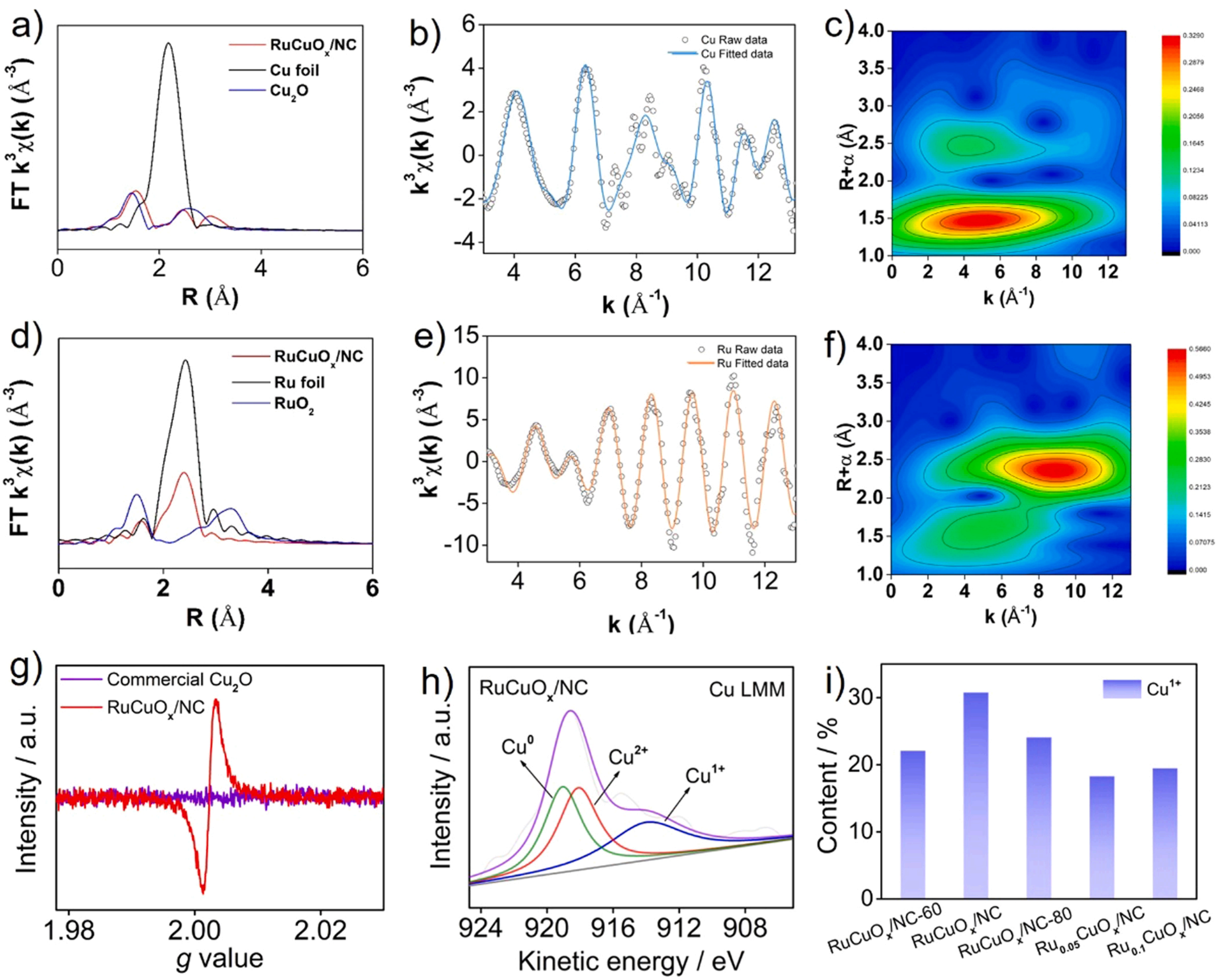

Fig. 4. a) R-spaced FT-EXAFS of Cu *K*-edge. b) k^3-weighted EXAFS oscillations of Cu *K*-edge. c) k^2-weighted WT-EXAFS plots of Cu. d) R-spaced FT-EXAFS of Ru *K*-edge. e) k^3-weighted EXAFS oscillations of Ru *K*-edge. f) k^2-weighted WT-EXAFS plots of Ru. g) EPR signals of $RuCuO_x$/NC and commercial Cu_2O. h) Cu LMM spectrum of $RuCuO_x$/NC. i) Cu^{1+} content of the catalysts calculated from Cu LMM spectra.

towards higher binding energy whilst the Cu 2p spectrum towards lower binding energy, indicating there existed electron transfer from Ru to Cu (Table S2-S3) [39,47]. The interaction between Ru and Cu-based constituents altered the electronic structures and the surface charge distribution, accompanied with the generation of more $Cu^{0/1+}$ states, which may optimize the adsorption bonding behavior of active sites to the reaction species. To be specific, during the hot-alkali corrosion process, part of metallic Cu was oxidized by NaOH to form $Cu_{2+1}O$ (Cu^{1+}) or CuO (Cu^{2+}). Nevertheless, owing to the interplay between Ru and Cu-based constituents, Ru was able to effectively prevent the peroxidation of Cu-based constituents, thus generating more $Cu^{0/1+}$ species. In our system, the increment of Cu^{1+} ratio may promote the HER [48,49]. From the above results, it is reasonable to infer that the introduction of Ru regulated the electronic structure of Cu, and thus might synergistically enhance the HER performance.

X-ray absorption fine structure (XAFS) of Cu *K*-edge and Ru *K*-edge was conducted to analyze the local coordination environment of Cu and Ru in $RuCuO_x$/NC. In the Fourier transformed extended X-ray absorption fine structure (FT-EXAFS) data of Cu *K*-edge (Fig. 4a), the first coordination peak in R-space at about 1.95 Å could be fitted to the first coordination shell of the Cu-O bond, and the second peak located at 2.87 Å was attributed to the higher shell of Cu-Cu scattering path [50]. The corresponding average coordination numbers (CNs) of Cu according to EXAFS data-fitting were listed in Table S4. The average CN of Cu–O in $RuCuO_x$/NC was 2.4, close to the standard samples of Cu_2O (1.9), indicating that the existence of Cu_2O in $RuCuO_x$/NC [42]. The slightly higher Cu–O coordination may be attributed to the partial oxidation of metallic copper or Cu_2O to CuO. Notably, the second shell CN of Cu-Cu was significantly lower than that of Cu_2O, manifesting the unsaturated coordination of Cu atoms and the appearance of oxygen vacancies surrounding Cu atoms in $RuCuO_x$/NC [51]. This further confirmed the formation of $Cu_{2+1}O$, which was well consistent with XRD (Fig. 3a). The k^2-weighted wavelet-transformed (WT) EXAFS (Fig. 4c) contour plots of $RuCuO_x$/NC showed a lobe at 4.2 $Å^{-1}$, 2.5 Å, which could be indexed to Cu-Cu coordination. The other lobe at about 4.9 $Å^{-1}$, 1.5 Å corresponded to the Cu-O coordination. As shown in the EXAFS spectra in *R* space of Ru *K*-edge (Fig. 4d), an intensive coordination peak at about 2.68 Å was observed, which coincided with the main peak of Ru foil. A relatively weak at about 2.00 Å was assigned to Ru-O shell. The EXAFS data-fitting results (Table S4) revealed that the CN of Ru-Ru path is 5.7, indicating that Ru atoms in $RuCuO_x$/NC mainly existed in the form of small Ru nanoparticles. The CN of 2.8 for Ru-O in the catalyst suggested the existence of oxidation state of Ru, which was probably due to the interaction between the Ru nanoparticles and CuO_x. This accorded well with the XPS results (Fig. 3). The presence of Ru–Ru and Ru-O scattering is further demonstrated by the WT technique. As shown in Fig. 4f, the catalyst afforded two lobes at (9.0 $Å^{-1}$, 2.4 Å) and (5.3 $Å^{-1}$, 1.6 Å), which were attributed to Ru-Ru and Ru-O contributions, respectively [52]. The local coordination environment around the Cu and Ru was expressed by the oscillations in the low k (3–13 $Å^{-1}$) with R factor of 0.018 and 0.011, indicating the accuracy of fitting results (Fig. 4b, 4e).

The defects were further probed by electron paramagnetic resonance (EPR). Commercial Cu_2O served as a reference to reveal the copper excess defects. As shown in Fig. 4g, no signal could be observed as for Cu_2O. In contrast, a distinct and strong peak at *g* value of 2.002 was presented in $RuCuO_x$/NC, indicating the formation of defects [53,54]. To further clarify the valence state of Cu, Cu LMM XAES was performed to exactly distinguish Cu^0 and Cu^{1+}. As revealed in Fig. 4h and Fig. S10, the binding energy at ~919 eV and ~914 eV corresponded to Cu^0 and Cu^{1+}, respectively [55].

3.3. Electrochemical performance and the origin of catalytic activity

The electrocatalytic activity of RuCu-based composites toward HER was assessed through a conventional three-electrode cell setup, which performed under 1 M KOH. To gain deep insights into the role of each component on the catalytic activity, NC, CuO_x/NC, Ru/NC, and $RuCuO_x$/NC-nL were also evaluated. From the linear sweep voltammetry (LSV) curves in Fig. 5a, NC showed negligible catalytic activity. When introducing Cu ingredient in the system, CuO_x/NC still remained chemically inert. However, the overpotential of Ru/NC obviously decreased to ~114 mV versus the reversible hydrogen electrode (RHE) owing to the reactive Ru for HER. Excitingly, upon introducing tiny Ru into the CuO_x/NC system, a significantly improved catalytic activity of $RuCuO_x$/NC was obtained, representing the collaborative effect of Ru and $Cu_{2+1}O$. To reach current density of 10 mA cm^{-2}, $RuCuO_x$/NC delivered low overpotential of ~29 mV, which was comparable to that of commercial Pt/C. In particular, the catalytic activity of $RuCuO_x$/NC also outbalanced the recently reported electrocatalysts toward alkaline HER (Fig. 5b and Table S6). However, comparing to $RuCuO_x$/NC, $RuCuO_x$/NC-nL presented much inferior activity due to the low specific surface area and the lack of $Cu_{2+1}O$. Electrochemical impedance spectrum (EIS) further revealed that $RuCuO_x$/NC possessed the smallest semicircle diameter, suggesting the smallest charge transfer resistance (R_{ct}), and corresponding to the fastest charge transfer rate (Fig. 5c) [56]. Such results clearly indicated that Ru activated the hydrogen production capacity of insert Cu-based catalysts, and Ru, $Cu_{2+1}O$ synergistically promoted the HER.

Therewith, a series of $RuCuO_x$-based hybrids with different Ru additions were constructed to systematically unveil the synergistic effect between Ru and $Cu_{2+1}O$ for HER. The established samples are denoted as $Ru_{0.05}CuO_x$/NC and $Ru_{0.1}CuO_x$/NC with the Ru element dosage as 0.05 mmol, 0.1 mmol. As can be seen in Fig. 5d, the catalytic activity gradually elevated and then drop off with increasing in the Ru dosage, which manifested that the appropriate Ru content played a crucial role in the optimization of the catalytic performance. EIS data demonstrated that the diameter of the Nyquist plots decreased progressively in the order of $Ru_{0.05}CuO_x$/NC, $Ru_{0.1}CuO_x$/NC to $RuCuO_x$/NC (Fig. 5e). The smaller diameter indicated the decreased R_{ct}, corresponding to the gradually increased catalytic performance. Moreover, the electrochemical active surface area (ECSA) is further employed to analyze the effective active surface area and the quantity of active sites, which was characterized by the double layer capacitances (C_{dl}) [57,58]. Electrocatalytic test disclosed that the rule of C_{dl} was consistent with the catalytic performance order (Fig. 5f, Fig. S11), following the sequence of $RuCuO_x$/NC (85.1 mF cm^{-2}) > $Ru_{0.1}CuO_x$/NC (59.5 mF cm^{-2}) > $Ru_{0.05}CuO_x$/NC (33.5 mF cm^{-2}). The large C_{dl} value signified the high ECSA. It indicated more active centers were exposed [59], which contributed to the salient HER property. To shed light on insights about the HER kinetic features, the Tafel slopes were gained from the linear part of the Tafel plots (Fig. 5g). The Tafel slopes of $Ru_{0.05}CuO_x$/NC, $RuCuO_x$/NC and $Ru_{0.1}CuO_x$/NC were calculated to be 126.0 mV dec^{-1}, 57.7 mV dec^{-1} and 89.8 mV dec^{-1}, respectively. The sharply smaller Tafel value suggested the favorable reaction kinetics. In the light of the HER mechanism in alkaline media, $RuCuO_x$/NC adhered to the Volmer-Heyrovsky pathway.

Based on the results of elemental analysis, $Ru_{0.05}CuO_x$/NC, $Ru_{0.1}CuO_x$/NC and $RuCuO_x$/NC possessed the similar N amount (Table S5), which excluded the effect of N doping on the activity. The following discussions elaborate the decisive factor of $RuCuO_x$/NC superiority over other reference catalysts in the kinetics of HER. XPS was employed to unveil the correlation between the distribution of each species and the catalytic activity. From the Ru 3p spectrum (Fig. S12a-b), $RuCuO_x$/NC and $Ru_{0.1}CuO_x$/NC possessed a similar percentage of Ru^0, which was significantly higher than that of $Ru_{0.05}CuO_x$/NC (Fig. 5h). The higher proportion of Ru^0 states contributed to the process of H_2O splitting under alkaline conditions, which accelerating the H_2 production [60]. However, although Ru/NC owned more Ru^0 state content, its catalytic activity was far from satisfactory comparing with that of $RuCuO_x$/NC. The findings indicated that the high Ru^0 content and Cu species co-existed enabled the catalyst to maximize catalytic performance. Based on the Cu $2p_{3/2}$ XPS spectra analysis (Fig. 5i and

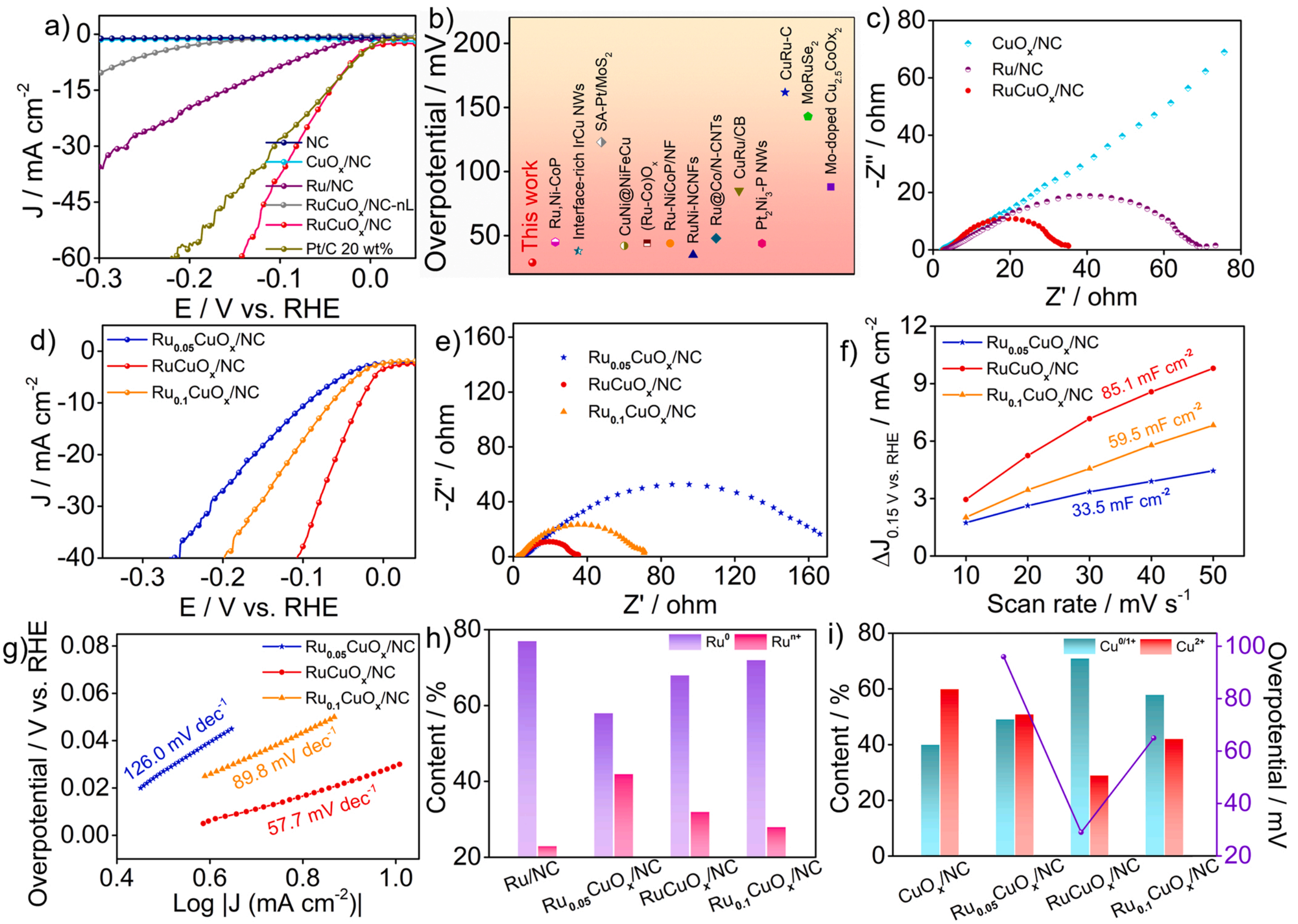

Fig. 5. a) LSV polarization curves of control samples, b) Comparation on the activity of $RuCuO_x/NC$ and the recently reported electrocatalysts, c) Nyquist plots for CuO_x/NC, Ru/NC and $RuCuO_x/NC$. Electrochemical data of $Ru_{0.05}CuO_x/NC$, $RuCuO_x/NC$ and $Ru_{0.1}CuO_x/NC$: d) LSV polarization curves, e) Nyquist plots, f) Double-layer capacitances, g) Tafel plots, h) Content distributions of each Ru species, i) Content distributions of each Cu species and the overpotential under 10 mA cm^{-2} for varied samples.

Fig. S12c-d), the $Cu^{0/1+}$ contents increased with the addition of $RuCl_3$ to a peak, then declined. The content distributions of $Cu^{0/1+}$ and the overpotential under 10 mA cm^{-2} for varied samples demonstrated that the higher content of $Cu^{0/1+}$, the better the catalytic performance. Furthermore, attempts to correlate the content of Cu^{1+} with the catalytic performance witnessed that the higher Cu^{1+} was conductive to improving the HER activity (Fig. 4i), further highlighting the vital role of Cu^{1+}. It has been recognized that $Cu_{2+1}O$ not only facilitates the charge transport, but also contributes to abundant active sites. Meanwhile, the free electrons from $Cu_{2+1}O$ ameliorates the reaction kinetics [61]. As a consequence, the collaborative effect between $Cu_{2+1}O$ (Cu^{1+}) and Ru^0 promoted the hydrogen production. Particularly, $Cu_{2+1}O$ phase significantly accelerated the catalytic performance, and hence, the functions of $Cu_{2+1}O$ were emphatically investigated.

From the above findings, the hot-alkali treatment is the paramount procedure to introduce the highly active $Cu_{2+1}O$ phase. With the attempt to gain deeper light on the influence of $Cu_{2+1}O$ on the catalytic process, we further designed catalysts treated by NaOH with different temperature to modulate the Cu bonding types (Fig. 6a). The hybrids produced by reaction with NaOH under 60 °C and 80 °C were named as $RuCuO_x/NC$-60 and $RuCuO_x/NC$-80 severally. According to the results of XRD patterns (Fig. 6b), diffraction peaks belonged to SiO_2 can be recognized in $RuCuO_x/NC$-60. And no obvious $Cu_{2+1}O$ phase was observed. While, upon elevating the temperature from 60 °C to 70 °C or 80 °C, SiO_2 was completely etched by NaOH. Moreover, the XRD patterns manifested that $RuCuO_x/NC$ and $RuCuO_x/NC$-80 displayed similar diffraction features, including a broad graphitic carbon peak and the typical characteristic diffraction peaks for metallic Cu and $Cu_{2+1}O$. Correspondingly, $RuCuO_x/NC$-60 presented much inferior performance under 10 mA cm^{-2} (~96 mV) than that of $RuCuO_x/NC$ (~29 mV) and $RuCuO_x/NC$-80 (~70 mV), which was ascribed to the tiny SiO_2 residues and the low content of $Cu_{2+1}O$ in $RuCuO_x/NC$-60 (Fig. 5c). On the one hand, the tiny SiO_2 residues lead to the decrease of the specific surface area of $RuCuO_x/NC$-60 (Table S1). The low specific surface area goes against the exposure of active sites and mass transfer. On the other hand, SiO_2 residues affect the conductivity of $RuCuO_x/NC$-60, which is manifested as a higher charge transfer resistance on the electrode surface (Fig. S13) [31]. More importantly, the catalytic activity has particularly close ties to the bonding configurations of Cu species. Specifically, when rising the temperature from 60 °C to 70 °C, more Cu^0 states were converted to Cu^{1+} states (Fig. 4i). The dominated Cu^{1+} ratio in $RuCuO_x/NC$ (Fig. 4i) enabled the outstanding HER activity. Further elevating the temperature to 80 °C, the $Cu^{0/1+}$ species was more facilely oxidized, thus resulting in the generation of more Cu^{2+}. The relative lower Cu^{1+} percentage gave rise to the unsatisfactory activity of $RuCuO_x/NC$-80. Given all that, these results were in good accordance with the above experimental findings, further confirming that the high Cu^{1+} content governed the prominent HER performance.

To further follow the origin of the catalytic activity, a series of $RuCuO_x/NC$ with different $Cu_{2+1}O$ contents were thereby constructed

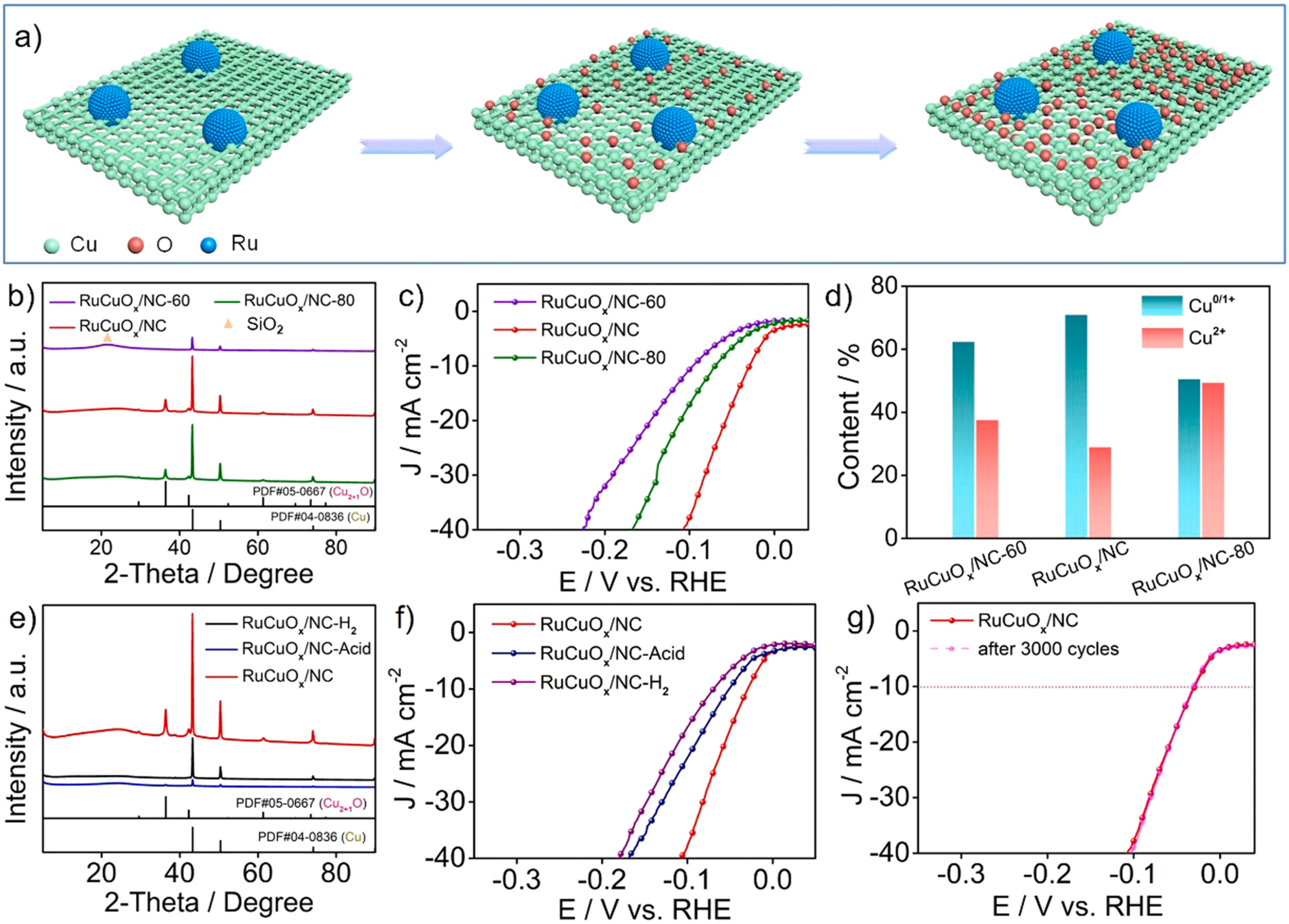

Fig. 6. a) Schematic diagram for the regulation of Cu-based constituents, b, c) XRD patterns and LSV plots of RuCuO$_x$/NC-60, RuCuO$_x$/NC and RuCuO$_x$/NC-80, d) Content distributions of each Cu species in RuCuO$_x$/NC-60, RuCuO$_x$/NC and RuCuO$_x$/NC-80, e, f) XRD patterns and LSV plots of RuCuO$_x$/NC, RuCuO$_x$/NC-Acid, RuCuO$_x$/NC-H$_2$, g) LSV polarization curves of RuCuO$_x$/NC recorded before and after 3000 CV scanning.

by means of acid etching and H_2 reduction. XRD observations demonstrated that there was still partial $Cu_{2+1}O$ residue even after long-term acidic treatment (Fig. 6e). It is difficult to completely remove $Cu_{2+1}O$ because of the confinement effect of the carbon nanotubes. Correspondingly, the activity obviously attenuated with the decline of $Cu_{2+1}O$ content (Fig. 6f). While, the diffraction peaks of $Cu_{2+1}O$ disappeared after H_2 reduction, indicating that $Cu_{2+1}O$ was completely reduced to metallic Cu. As expected, to drive current density of 10 mA cm^{-2}, the overpotential of RuCuO$_x$/NC-H$_2$ further rose from ~29 mV to ~65 mV with the deficiency of $Cu_{2+1}O$ phase. Additionally, RuCuO$_x$/NC-nL was also obviously etched and oxidized after hot-alkali reaction, which regulated the $Cu_{2+1}O$ content. Compared with RuCuO$_x$/NC-nL, the catalytic activity significantly enhanced after RuCuO$_x$/NC-nL treating by NaOH (Fig. S15), which was attributed to the introduction of active $Cu_{2+1}O$. From the above results, we have reasons to believe that $Cu_{2+1}O$ plays a decisive role in improving the catalytic activity.

Apart from the catalytic activity, stability is another essential indicator to be considered for the design of an advanced HER catalyst. Whereafter, the stability of RuCuO$_x$/NC was evaluated via cyclic voltammetry (CV) test. For comparison, the stability of Ru/NC was tested as well. Following with the consecutive 3000 CV scanning, the overpotential of Ru/NC displayed an evident negative shift of ~37 mV at 10 mA cm^{-2} (Fig. S16). By sharp contrast, the catalytic performance exhibited negligible loss for RuCuO$_x$/NC (Fig. 6g), demonstrating the introduction of Cu also stabilized the Ru constituent and resulted in the promoted stability. In order to investigate the flexible of the catalyst, we also evaluated the catalytic performance in neutral medium. As expected, RuCuO$_x$/NC displayed superior performance with a low overpotential of 125 mV to achieve 10 mA cm^{-2} in neutral solution (Fig. S17).

To deeply comprehend into the origin for the superior performance, DFT calculations were carried out in the Vienna ab initio simulation package. As for the HER pathway under alkaline condition, it involves the initial dissociation of H_2O to H* and OH$^-$ and subsequent generation of H_2. Generally, free energy of water dissociation (ΔG_{H2O}) and free energy of adsorbed H intermediates (ΔG_{H*}) are functioned as activity descriptor to probe the catalytic efficiency [62]. A superior alkaline HER electrocatalysts should be able to accelerate the dissociation of H_2O into adsorbed OH and H, and provide moderate adsorption/desorption ability for H intermediate. Here, model systems including Ru/Cu, Ru/CuO, Ru/Cu_2O, Ru/$Cu_{2+1}O$, and the correlative optimized adsorption configurations of adsorbed OH and H and H* on the models were set up (Fig. 7a and Fig. S18). The ΔG_{H2O} for Ru/Cu and Ru/CuO was significantly higher than that of Ru/Cu_2O and Ru/$Cu_{2+1}O$ (Fig. 7b). The high ΔG_{H2O} will hinder the H_2O dissociation and lead to sluggish HER kinetics [63]. Therefore, the H_2O dissociation is more easily carried out on Ru/Cu_2O and Ru/$Cu_{2+1}O$ due to the lower value of ΔG_{H2O}. Although Ru/Cu_2O and Ru/$Cu_{2+1}O$ exhibited similar ΔG_{H2O}, Ru/$Cu_{2+1}O$ model with excess Cu sites showed lower $|\Delta G_{H*}|$ (0.18 eV) than Ru/$Cu_{2+1}O$ (0.30 eV), which endowed Ru/$Cu_{2+1}O$ with a thermodynamically favorable equilibrium between H* adsorption and desorption. The closer the ΔG_{H*} value is to the optimal value (ΔG_{H*}=0 eV), the better the

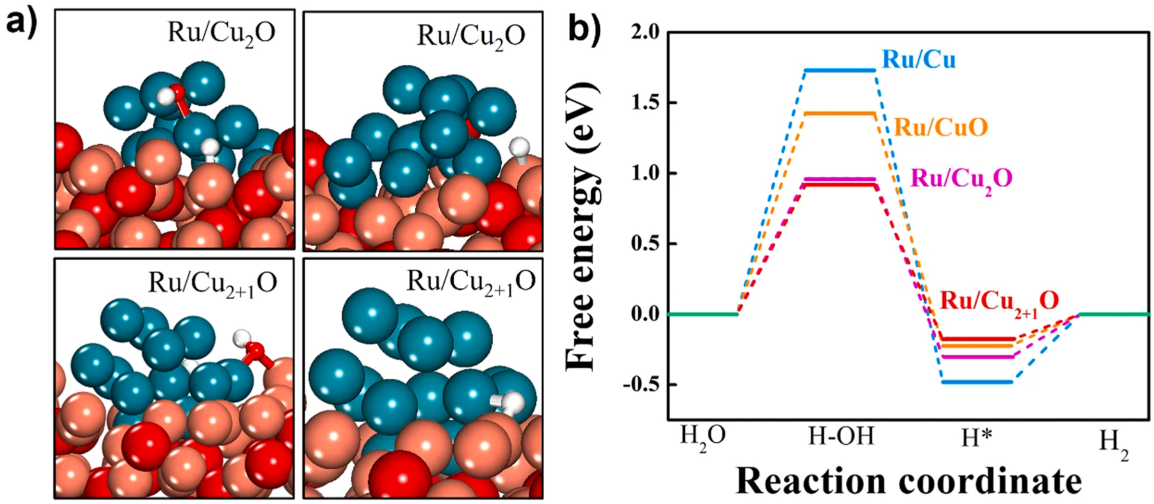

Fig. 7. a) The optimal (H-OH)* and H* absorption configuration for Ru/Cu_2O and Ru/$Cu_{2+1}O$. b) The corresponding free energy diagram for HER of Ru/Cu, Ru/CuO, Ru/Cu_2O and Ru/$Cu_{2+1}O$ under the alkaline condition. Color code: Ru (green), Cu (orange), O (red), H (white).

activity is. The better catalytic performance of Ru/$Cu_{2+1}O$ emphasized the important role of oxygen vacancies in boosting the HER performance. The higher value of $|\Delta G_{H^*}|$ for Ru/Cu and Ru/CuO implied the strong adsorption to H*, which further deteriorated the HER process. Remarkably, calculation results also indicated that the H* prefer to absorb at the interface site between Cu and Ru from the Ru/$Cu_{2+1}O$ configuration, further revealed that the Ru/$Cu_{2+1}O$ interface functioned as the active centers. Thus, these findings certified that the introduction of $Cu_{2+1}O$ layers could promote the reaction and the synergistic effect of $Cu_{2+1}O$ and Ru guaranteed the superior performance for HER.

4. Conclusion

To sum up, highly active RuCu-based electrocatalysts were facilely designed by dual-templates assembling-pyrolysis-alkali etching strategy. In our system, the Ludox template promoted the mesoporous formation, while the CTAB template acted as a structure-directing agent, metal dispersant and stabilizer, and both of them collaboratively contributes to the construction of efficient catalysts. Significantly, the reactive $Cu_{2+1}O$ layer was introduced via the alkali-etching process. As expected, the established $RuCuO_x$/NC delivered a Pt-like HER performance with fast reaction kinetics, outstanding activity and stability under alkaline electrolytes. Experimental investigation manifested that the appropriate Ru addition optimized the electronic structure of Cu phase. The interplay between Ru and Cu effectively promoted the formation of $Cu^{0/1+}$ states. The synergistic effect between the dominated Cu^{1+} configurations and Ru^0 state are favorable over the hydrogen generation. Furthermore, DFT results rationalized that the synergistic cooperation of $Cu_{2+1}O$ and Ru significantly accelerated H_2O dissociation and lowered the hydrogen adsorption energy to thermodynamically favorable equilibrium between H* adsorption and desorption. This work proposed a promising methodology to construct multicomponent electrocatalysts, which may lend perspective for the rational design of advanced electrocatalysts for renewable energy systems.

CRediT authorship contribution statement

Jing Wang: Investigation, Methodology, Writing – original draft, Funding acquisition. **Bingxin Guo:** Formal analysis, Investigation, Visualization. **Junting Sun:** Investigation. **Yingshuang Zhou:** Investigation. **Chengfei Zhao:** Investigation. **Zhongzhe Wei:** Conceptualization, Methodology, Writing – review & editing, Funding acquisition. **Junjie Guo:** Conceptualization, Writing -– review & editing, Project administration.

Declaration of Competing Interest

The authors declare that they have no known competing financial interests or personal relationships that could have appeared to influence the work reported in this paper.

Data Availability

Data will be made available on request.

Acknowledgements

This work was supported by the National Natural Science Foundation of China (52002102, 22008213), the Zhejiang Provincial Natural Science Foundation (LQ21B060005, LQ19B030009) and the Fundamental Research Funds for the Provincial Universities of Zhejiang (RF-A2022011).

Appendix A. Supporting information

Supplementary data associated with this article can be found in the online version at doi:10.1016/j.apcatb.2022.122169.

References

[1] Louis Schlapbach, Technology hydrogen-fuelled vehicles, Nature 460 (2009) 809–811, https://doi.org/10.1038/460809a.
[2] Jing Zhu, Liangsheng Hu, Pengxiang Zhao, Lawrence Yoon, Suk Lee, Kwok-Yin Wong, Recent advances in electrocatalytic hydrogen evolution using nanoparticles, Chem. Rev. 120 (2020) 851–918, https://doi.org/10.1021/acs.chemrev.9b00248.
[3] Arthur J. Shih, Sossina M. Haile, Electrifying membranes to deliver hydrogen An electrochemical membrane reactor enables efficient hydrogen generation, Science 376 (2022) 348–349, https://doi.org/10.1126/science.abo5369.
[4] Yinlong Zhu, Qian Lin, Yijun Zhong, Hassan A. Tahini, Zongping Shao, Huanting Wang, Metal oxide-based materials as an emerging family of hydrogen evolution electrocatalysts, Energy Environ. Sci. 13 (2020) 3361–3392, https://doi.org/10.1039/d0ee02485f.
[5] Nam Khen Oh, Jihyung Seo, Sangjin Lee, Hyung-Jin Kim, Ungsoo Kim, Junghyun Lee, Young-Kyu Han, Hyesung Park, Highly efficient and robust noble-metal free bifunctional water electrolysis catalyst achieved via complementary charge transfer, Nat. Commun. 12 (2021) 4606, https://doi.org/10.1038/s41467-021-24829-8.
[6] Jiarui Yang, Wen-Hao Li, Shengdong Tan, Kaini Xu, Yu Wang, Dingsheng Wang, Yadong Li, The electronic metal-support interaction directing the design of single atomic site catalysts: achieving high efficiency towards hydrogen evolution, Angew. Chem. Int. Ed. 60 (2021) 19085–19091, https://doi.org/10.1002/anie.202107123.
[7] Jiadong Chen, Minkai Qin, Shuangxiu Ma, Ruxue Fan, Xiaozhong Zheng, Shanjun Mao, Chunhong Chen, Yong Wang, Rational construction of Pt/PtTex

interface with optimal intermediate adsorption energy for efficient hydrogen evolution reaction, Appl. Catal. B Environ. 299 (2021), 120640, https://doi.org/10.1016/j.apcatb.2021.120640.
[8] Jun Mei, Tianwei He, Juan Bai, Dongchen Qi, Aijun Du, Ting Liao, Godwin A. Ayoko, Yusuke Yamauchi, Litao Sun, Ziqi Sun, Surface-dependent intermediate adsorption modulation on iridium-modified black phosphorus electrocatalysts for efficient pH-universal water splitting, Adv. Mater. 33 (2021), 2104638, https://doi.org/10.1002/adma.202104638.
[9] Shangqian Zhu, Xueping Qin, Fei Xiao, Shuangli Yang, Yuan Xu, Zhuo Tan, Jiadong Li, Jiawei Yan, Qing Chen, Mingshu Chen, Minhua Shao, The role of ruthenium in improving the kinetics of hydrogen oxidation and evolution reactions of platinum, Nat. Catal. 4 (2021) 711–718, https://doi.org/10.1038/s41929-021-00663-5.
[10] Hanhui You, Dongshuang Wu, Duanhui Si, Minna Cao, Fanfei Sun, Hao Zhang, HuiMin Wang, Tian-Fu Liu, Rong Cao, Monolayer niir-layered double hydroxide as a long-lived efficient oxygen evolution catalyst for seawater splitting, J. Am. Chem. Soc. (2022), https://doi.org/10.1021/jacs.2c00242.
[11] Zi-You Yu, Yu Duan, Xing-Yu Feng, Xingxing Yu, Min-Rui Gao, Shu-Hong Yu, Clean and affordable hydrogen fuel from alkaline water splitting: past, recent progress, and future prospects, Adv. Mater. 33 (2021), 2007100, https://doi.org/10.1002/adma.202007100.
[12] Zhongzhe Wei, Zijiang Zhao, Jing Wang, Qiang Zhou, Chenxia Zhao, Zihao Yao, Jianguo Wang, Oxygen-deficient TiO_2 and carbon coupling synergistically boost the activity of Ru nanoparticles for the alkaline hydrogen evolution reaction, J. Mater. Chem. A 9 (2021) 10160–10168, https://doi.org/10.1039/d0ta11986e.
[13] Jiadong Chen, Chunhong Chen, Yuzhuo Chen, Haiyan Wang, Shanjun Mao, Yong Wang, Improving alkaline hydrogen evolution reaction kinetics on molybdenum carbide: Introducing Ru dopant, J. Catal. 392 (2020) 313–321, https://doi.org/10.1016/j.jcat.2020.10.020.
[14] Filip Podjaski, Daniel Weber, Siyuan Zhang, Leo Diehl, Roland Eger, Viola Duppel, Esther Alarcon-Llado, Gunther Richter, Frederik Haase, Anna Fontcuberta i Morral, Christina Scheu, Bettina V. Lotsch, Rational strain engineering in delafossite oxides for highly efficient hydrogen evolution catalysis in acidic media, Nat. Catal. 3 (2020) 55–63, https://doi.org/10.1038/s41929-019-0400-x.
[15] F. Rosalbino, D. Maccio, E. Angelini, A. Saccone, S. Delfino, Electrocatalytic properties of Fe-R (R = rare earth metal) crystalline alloys as hydrogen electrodes in alkaline water electrolysis, J. Alloy. Compd. 403 (2005) 275–282, https://doi.org/10.1016/j.jallcom.2005.03.075.
[16] Peng Zhou, Li Tao, Shasha Tao, Yinchang Li, Dongdong Wang, Xinwei Dong, Thomas Frauenheim, Xianzhu Fu, Xingshuai Lv, Shuangyin Wang, Construction of nickel-based dual heterointerfaces towards accelerated alkaline hydrogen evolution via boosting multi-step elementary reaction, Adv. Funct. Mater. 31 (2021), 2104827, https://doi.org/10.1002/adfm.202104827.
[17] Dongjoon Kim, Yuhyeon Lee, Minkyu Kim, Gibaek Lee, Shrine Maria, Nithya Jeghan, Designing a smart heterojunction coupling of cobalt-iron layered double hydroxide on nickel selenide nanosheets for highly efficient overall water splitting kinetics, Appl. Catal. B Environ. 308 (2022), 121221, https://doi.org/10.1016/j.apcatb.2022.121221.
[18] Sundaram Chandrasekaran, Mahima Khandelwal, Fan Dayong, Lijun Sui, Jin Suk Chung, R.D.K. Misra, Peng Yin, Eui Jung Kim, Woong Kim, Aravindan Vanchiappan, Yongping Liu, Seung Hyun Hur, Han Zhang, Chris Bowen, Developments and perspectives on robust nano- and microstructured binder-free electrodes for bifunctional water electrolysis and beyond, Adv. Energy Mater. (2022), 2200409, https://doi.org/10.1002/aenm.202200409.
[19] Fan Liu, Chengxiang Shi, Xiaolei Guo, Zexing He, Lun Pan, Zhen-Feng Huang, Xiangwen Zhang, Ji-Jun Zou, Rational design of better hydrogen evolution electrocatalysts for water splitting: a review, Adv. Sci. (2022), 2200307, https://doi.org/10.1002/advs.202200307.
[20] Huanyu Jin, Huimin Yu, Haobo Li, Kenneth Davey, Taeseup Song, Ungyu Paik, Shi-Zhang Qiao, MXene analogue: a 2D nitridene solid solution for high-rate hydrogen production, Angew. Chem. Int. Ed. (2022), e202203850, https://doi.org/10.1002/anie.202203850.
[21] Hao Wang, Xu Xiao, Shuyuan Liu, Chao-Lung Chiang, Xiaoxiao Kuai, Chun-Kuo Peng, Yu-Chang Lin, Xing Meng, Jianqing Zhao, Jinho Choi, Yan-Gu Lin, Jong-Min Lee, Lijun Gao, Structural and electronic optimization of MoS_2 edges for hydrogen evolution, J. Am. Chem. Soc. 141 (2019) 18578–18584, https://doi.org/10.1021/jacs.9b09932.
[22] Yan Wang, Yao Nian, Akash N. Biswas, Wei Li, You Han, Jingguang G. Chen, Challenges and opportunities in utilizing MXenes of carbides and nitrides as electrocatalysts, Adv. Energy Mater. 11 (2021), 2002967, https://doi.org/10.1002/aenm.202002967.
[23] Ge Wang, Jingying Tao, Yijie Zhang, Shengping Wang, Xiaojun Yan, Congcong Liu, Fei Hu, Zhiying He, Zhijun Zuo, Xiaowei Yang, Engineering two-dimensional mass-transport channels of the MoS_2 nanocatalyst toward improved hydrogen evolution performance, ACS Appl. Mater. Interfaces 10 (2018) 25409–25414, https://doi.org/10.1021/acsami.8b07163.
[24] Binbin Lin, Jiadong Chen, Rui Yang, Shanjun Mao, Minkai Qin, Yong Wang, Multi-hierarchical cobalt-based electrocatalyst towards high rate H_2 production, Appl. Catal. B Environ. 316 (2022), 121666, https://doi.org/10.1016/j.apcatb.2022.121666.
[25] Jeff Greeley, Thomas F. Jaramillo, Jacob Bonde, I.B. Chorkendorff, Jens K. Norskov, Computational high-throughput screening of electrocatalytic materials for hydrogen evolution, Nat. Mater. 5 (2006) 909–913, https://doi.org/10.1038/nmat1752.
[26] Jing Wang, Ting Liao, Zhongzhe Wei, Junting Sun, Junjie Guo, Ziqi Sun, Heteroatom-doping of non-noble metal-based catalysts for electrocatalytic hydrogen evolution: an electronic structure tuning strategy, Small Methods 5 (2021), 2000988, https://doi.org/10.1002/smtd.202000988.
[27] Dong Cao, Haoxiang Xu, Daojian Cheng, Branch-leaf-shaped CuNi@NiFeCu nanodendrites as highly efficient electrocatalysts for overall water splitting, Appl. Catal. B Environ. 298 (2021), 120600, https://doi.org/10.1016/j.apcatb.2021.120600.
[28] Khadim Shah, Ruoyun Dai, Muhammad Mateen, Zubair Hassan, Zewen Zhuang, Chuhao Liu, Muhammad Israr, Weng-Chon Cheong, Botao Hu, Renyong Tu, Chao Zhang, Xin Chen, Qing Peng, Chen Chen, Yadong Li, Cobalt single atom incorporated in ruthenium oxide sphere: a robust bifunctional electrocatalyst for HER and OER, Angew. Chem. Int. Ed. 61 (2022), https://doi.org/10.1002/anie.202114951.
[29] Tianjie Qiu, Zibin Liang, Wenhan Guo, Song Gao, Chong Qu, Hassina Tabassum, Hao Zhang, Bingjun Zhu, Ruqiang Zou, Shao-Horn Yang, Highly exposed ruthenium-based electrocatalysts from bimetallic metal-organic frameworks for overall water splitting, Nano Energy 58 (2019) 1–10, https://doi.org/10.1016/j.nanoen.2018.12.085.
[30] Yong-Ya Zhang, Nan Zhang, Peng Peng, Rui Wang, Yan Jin, Ya-Kun Lv, Xin Wang, Wei Wei, Shuang-Quan Zang, Uniformly dispersed Ru nanoparticles constructed by in situ confined polymerization of ionic liquids for the electrocatalytic hydrogen evolution reaction, Small Methods 5 (2021), 2100505, https://doi.org/10.1002/smtd.202100505.
[31] Do. Hyung Kweon, Mahmut Sait Okyay, Seok-Jin Kim, Jong-Pil Jeon, Hyuk-Jun Noh, Noejung Park, Javeed Mahmood, Jong-Beom Baek, Ruthenium anchored on carbon nanotube electrocatalyst for hydrogen production with enhanced Faradaic efficiency, Nat. Commun. 11 (2020) 1278, https://doi.org/10.1038/s41467-020-15069-3.
[32] Jing Wang, Zhongzhe Wei, Shanjun Mao, Haoran Li, Yong Wang, Highly uniform Ru nanoparticles over N-doped carbon: pH and temperature-universal hydrogen release from water reduction, Energy Environ. Sci. 11 (2018) 800–806, https://doi.org/10.1039/c7ee03345a.
[33] Weidong Li, Yunxuan Zhao, Yuan Liu, Mingzi Sun, Geoffrey I.N. Waterhouse, Bolong Huang, Kan Zhang, Tierui Zhang, Siyu Lu, Exploiting Ru-induced lattice strain in CoRu nanoalloys for robust bifunctional hydrogen production, Angew. Chem. Int. Ed. 60 (2021) 3290–3298, https://doi.org/10.1002/anie.202013985.
[34] Junmeng Zhang, Xiaopei Xu, Liu Yang, Daojian Cheng, Dapeng Cao, Single-atom Ru doping induced phase transition of MoS_2 and S vacancy for hydrogen evolution reaction, Small Methods 3 (2019), 1900653, https://doi.org/10.1002/smtd.201900653.
[35] Chengli Rong, Xiangjian Shen, Yuan Wang, Lars Thomsen, Tingwen Zhao, Yibing Li, Xunyu Lu, Rose Amal, Chuan Zhao, Electronic structure engineering of single-atom Ru sites via Co-N_4 sites for bifunctional pH-universal water splitting, Adv. Mater. (2022), 2110103, https://doi.org/10.1002/adma.202110103.
[36] Yingjie Yang, Daoxiong Wu, Ruisong Li, Peng Rao, Jing Li, Peilin Deng, Junming Luo, Wei Huang, Qi Chen, Zhenye Kang, Yijun Shen, Xinlong Tian, Engineering the strong metal support interaction of titanium nitride and ruthenium nanorods for effective hydrogen evolution reaction, Appl. Catal. B Environ. (2022), 121796, https://doi.org/10.1016/j.apcatb.2022.121796.
[37] Chuang Li, Haeseong Jang, Min Gyu Kim, Liqiang Hou, Xien Liu, Jaephil Cho, Ru-incorporated oxygen-vacancy-enriched MoO_2 electrocatalysts for hydrogen evolution reaction, Appl. Catal. B Environ. 307 (2022), 121204, https://doi.org/10.1016/j.apcatb.2022.121204.
[38] Bingzhang Lu, Lin Guo, Feng Wu, Yi Peng, Jia En Lu, Tyler J. Smart, Nan Wang, Y. Zou Finfrock, David Morris, Peng Zhang, Ning Li, Peng Gao, Yuan Ping, Shaowei Chen, Ruthenium atomically dispersed in carbon outperforms platinum toward hydrogen evolution in alkaline media, Nat. Commun. 10 (2019) 631, https://doi.org/10.1038/s41467-019-08419-3.
[39] Qing Yao, Bolong Huang, Nan Zhang, Mingzi Sun, Qi Shao, Xiaoqing Huang, Channel-rich RuCu nanosheets for pH-universal overall water splitting electrocatalysis, Angew. Chem. Int. Ed (2019) 13983–13988, https://doi.org/10.1002/anie.201908092.
[40] Jing Gao, Liu Yang, Di Wang, Dapeng Cao, Hollow nanotube Ru/$Cu_{2+1}O$ supported on copper foam as a bifunctional catalyst for overall water splitting, Chem. Eur. J. 26 (2020) 4112–4119, https://doi.org/10.1002/chem.201904337.
[41] Songfang Zhao, Fei Han, Jinhui Li, Xiangying Meng, Wangping Huang, Duxia Cao, Guoping Zhang, Rong Sun, Ching-Ping Wong, Advancements in copper nanowires: synthesis, purification, assemblies, surface modification, and applications, Small 14 (2018), 1800047, https://doi.org/10.1002/smll.201800047.
[42] Jiajun Wang, Tingjun Fu, Fanhui Meng, Dan Zhao, Steven S.C. Chuang, Zhong Li, Highly active catalysis of methanol oxidative carbonylation over nano Cu_2O supported on micropore-rich mesoporous carbon, Appl. Catal. B Environ. 303 (2022), 120890, https://doi.org/10.1016/j.apcatb.2021.120890.
[43] Zhao Sun, Xianhua Zhang, Hongfang Li, Tao Liu, Sier Sang, Shiyi Chen, Lunbo Duan, Liang Zeng, Wenguo Xiang, Jinlong Gong, Chemical looping oxidative steam reforming of methanol: a new pathway for auto-thermal conversion, Appl. Catal. B Environ. 269 (2020), 118758, https://doi.org/10.1016/j.apcatb.2020.118758.
[44] Minghui Tang, Jiang Deng, Mingming Li, Xuefeng Li, Haoran Li, Zhirong Chen, Yong Wang, 3D-interconnected hierarchical porous N-doped carbon supported ruthenium nanoparticles as an efficient catalyst for toluene and quinoline hydrogenation, Green Chem. 18 (2016) 6082–6090, https://doi.org/10.1039/c6gc01858k.
[45] Shanyong Chen, Shiyan Wang, Panpan Hao, Muhong Li, Yu Zhang, Jia Guo, Weiping Ding, Min Liu, Jinlan Wang, Xuefeng Guo, N,O-C Nanocage-mediated high-efficient hydrogen evolution reaction on IrNi@N,O-C electrocatalyst, Appl.

Catal. B Environ. 304 (2022), 120996, https://doi.org/10.1016/j.apcatb.2021.120996.
[46] Di Li, Yiming Huang, Zengyong Li, Linxin Zhong, Chuanfu Liu, Xinwen Peng, Deep eutectic solvents derived carbon-based efficient electrocatalyst for boosting H_2 production coupled with glucose oxidation, Chem. Eng. J. 430 (2022), 132783, https://doi.org/10.1016/j.cej.2021.132783.
[47] Dong Cao, Jiayi Wang, Haoxiang Xu, Daojian Cheng, Growth of highly active amorphous RuCu nanosheets on Cu nanotubes for the hydrogen evolution reaction in wide pH values, Small 16 (2020), 2000924, https://doi.org/10.1002/smll.202000924.
[48] Manyu Liu, Jianzhi Wang, Qifeng Tian, Yiheng Liu, Pan Li, Wei Li, Ning Cai, Yanan Xue, Weimin Chen, Faquan Yu, Mo-doped Cu/Co hybrid oxide nanoarrays: an enhanced electrocatalytic performance for the hydrogen evolution reaction, ChemElectroChem 6 (2019) 1738–1744, https://doi.org/10.1002/celc.201801790.
[49] Yen-Hsun Su, Shi-Hong Huang, Po-Yen Kung, Tin-Wei Shen, Wen-Lin Wang, Hydrogen generation of Cu_2O nanoparticles/MnO-MnO_2 nanorods heterojunction supported on sonochemical-assisted synthesized few-layer graphene in water-splitting photocathode, ACS Sustain. Chem. Eng. 3 (2015) 1965–1973, https://doi.org/10.1021/acssuschemeng.5b00579.
[50] Chong Wang, Bin Ma, Simin Xu, Dapeng Li, Shan He, Yufei Zhao, Jingbin Han, Min Wei, David G. Evans, Xue Duan, Visible-light-driven overall water splitting with a largely-enhanced efficiency over a Cu2O@ZnCr-layered double hydroxide photocatalyst, Nano Energy 32 (2017) 463–469, https://doi.org/10.1016/j.nanoen.2017.01.010.
[51] Zhengxiang Gu, Na Yang, Peng Han, Min Kuang, Bingbao Mei, Zheng Jiang, Jun Zhong, Li Li, Gengfeng Zheng, Oxygen vacancy tuning toward efficient electrocatalytic CO_2 reduction to C_2H_4, Small Methods 3 (2019), 1800449, https://doi.org/10.1002/smtd.201800449.
[52] Wei Liu, Haisong Feng, Yusen Yang, Yiming Niu, Lei Wang, Pan Yin, Song Hong, Bingsen Zhang, Xin Zhang, Min Wei, Highly-efficient RuNi single-atom alloy catalysts toward chemoselective hydrogenation of nitroarenes, Nat. Commun. 13 (2022) 3188, https://doi.org/10.1038/s41467-022-30536-9.
[53] Qinglong Wang, Renfeng Dong, Qianxian Yang, Jiajia Wang, Shuyu Xu, Yuepeng Cai, Highly efficient visible-light-driven oxygen-vacancy-based $Cu_{2+1}O$ micromotors with biocompatible fuels, Nanoscale Horiz. 5 (2020) 325–330, https://doi.org/10.1039/c9nh00592g.
[54] Ganggang Li, Kai He, Fenglian Zhang, Guoxia Jiang, Zeyu Zhao, Zhongshen Zhang, Jie Cheng, Zhengping Hao, Defect enhanced CoMnNiOx catalysts derived from spent ternary lithium-ion batteries for low-temperature propane oxidation, Appl. Catal. B Environ. 309 (2022), 121231, https://doi.org/10.1016/j.apcatb.2022.121231.
[55] Xu Wu, Hao Meng, Yali Du, Jiangning Liu, Benhui Hou, Xianmei Xie, Insight into Cu_2O/CuO collaboration in the selective catalytic reduction of NO with NH_3: enhanced activity and synergistic mechanism, J. Catal. 384 (2020) 72–87, https://doi.org/10.1016/j.jcat.2020.01.025.
[56] Xiaozhong Zheng, Minkai Qin, Shuangxiu Ma, Yuzhuo Chen, Honghui Ning, Rui Yang, Shanjun Mao, Yong Wang, Strong oxide-support interaction over IrO_2/V_2O_5 for efficient pH-universal water splitting, Adv. Sci. 9 (2022), 2104636, https://doi.org/10.1002/advs.202104636.
[57] Jingting Zhu, Yudi Tu, Lejuan Cai, Haibin Ma, Yang Chai, Lifu Zhang, Wenjing Zhang, Defect-assisted anchoring of Pt single atoms on MoS_2 nanosheets produces high-performance catalyst for industrial hydrogen evolution reaction, Small 18 (2022), 2104824, https://doi.org/10.1002/smll.202104824.
[58] Yuyan Song, Jianlin Cheng, Jiang Liu, Qing Ye, Xiang Gao, Jinjun Lu, Yongliang Cheng, Modulating electronic structure of cobalt phosphide porous nanofiber by ruthenium and nickel dual doping for highly-efficiency overall water splitting at high current density, Appl. Catal. B Environ. 298 (2021), 120488, https://doi.org/10.1016/j.apcatb.2021.120488.
[59] Jingying Tao, Yijie Zhang, Shengping Wang, Ge Wang, Fei Hu, Xiaojun Yan, Lifeng Hao, Zhijun Zuo, Xiaowei Yang, Activating three-dimensional networks of Fe@Ni nanofibers via fast surface modification for efficient overall water splitting, ACS Appl. Mater. Interfaces 11 (2019) 18342–18348, https://doi.org/10.1021/acsami.9b01431.
[60] Meixuan Li, Huiyuan Wang, Wendong Zhu, Weimo Li, Ce Wang, Xiaofeng Lu, RuNi nanoparticles embedded in N-doped carbon nanofibers as a robust bifunctional catalyst for efficient overall water splitting, Adv. Sci. 7 (2020), 1901833, https://doi.org/10.1002/advs.201901833.
[61] Xueying Cao, Liang Cui, Bingping Liu, Ying Liu, Dedong Jia, Wenrong Yang, Joselito M. Razal, Jingquan Liu, Reverse synthesis of star anise-like cobalt doped Cu-MOF/$Cu_{2+1}O$ hybrid materials based on a $Cu(OH)_2$ precursor for high performance supercapacitors, J. Mater. Chem. A 7 (2019) 3815–3827, https://doi.org/10.1039/c8ta11396c.
[62] H. Li, X.L. Zhao, H.L. Liu, S. Chen, X.F. Yang, C.X. Lv, H.W. Zhang, X.L. She, D. J. Yang, Sub-1.5 nm ultrathin CoP nanosheet aerogel: efficient electrocatalyst for hydrogen evolution reaction at all pH values, Small 14 (2018), 1802824, https://doi.org/10.1002/smll.201802824.
[63] J.W. Liu, G.Z. Ding, J.Y. Yu, X.U. Liu, X.F. Zhang, J.J. Guo, J.C. Zhang, W. Ren, R. C. Che, Visualizing spatial potential and charge distribution in Ru/N-doped carbon electrocatalysts for superior hydrogen evolution reaction, J. Mater. Chem. A 7 (2019) 18072–18080, https://doi.org/10.1039/c9ta06206h.